Delft University of Technology

Model improvements to simulate charging in scanning electron microscope

Arat, Kerim T.; Klimpel, Thomas; Hagen, Cornelis W.

DOI
10.1117/1.JMM.18.4.044003

Publication date
2019

Document Version
Final published version

Published in
Journal of Micro/ Nanolithography, MEMS, and MOEMS

Citation (APA)
Arat, K. T., Klimpel, T., & Hagen, C. W. (2019). Model improvements to simulate charging in scanning electron microscope. *Journal of Micro/ Nanolithography, MEMS, and MOEMS*, *18*(4), 14. Article 044003. https://doi.org/10.1117/1.JMM.18.4.044003

Important note
To cite this publication, please use the final published version (if applicable).
Please check the document version above.

Copyright
Other than for strictly personal use, it is not permitted to download, forward or distribute the text or part of it, without the consent of the author(s) and/or copyright holder(s), unless the work is under an open content license such as Creative Commons.

Takedown policy
Please contact us and provide details if you believe this document breaches copyrights.
We will remove access to the work immediately and investigate your claim.

This work is downloaded from Delft University of Technology.
For technical reasons the number of authors shown on this cover page is limited to a maximum of 10.

Journal of
Micro/Nanolithography,
MEMS, and MOEMS

Nanolithography.SPIEDigitalLibrary.org

Model improvements to simulate charging in scanning electron microscope

Kerim T. Arat
Thomas Klimpel
Cornelis W. Hagen

SPIE.

Kerim T. Arat, Thomas Klimpel, Cornelis W. Hagen, "Model improvements to simulate charging in scanning electron microscope," *J. Micro/Nanolith. MEMS MOEMS* **18**(4), 044003 (2019), doi: 10.1117/1.JMM.18.4.044003.

Downloaded From: https://www.spiedigitallibrary.org/journals/Journal-of-Micro/Nanolithography,-MEMS,-and-MOEMS on 06 Feb 2020
Terms of Use: https://www.spiedigitallibrary.org/terms-of-use

J. Micro/Nanolith. MEMS MOEMS 18(4), 044003 (Oct–Dec 2019)

Model improvements to simulate charging in scanning electron microscope

Kerim T. Arat,[a,*] Thomas Klimpel,[b] and Cornelis W. Hagen[a]
[a]Delft University of Technology, Faculty of Applied Sciences, Delft, The Netherlands
[b]GenISys GmbH, Taufkirchen, Munich, Germany

Abstract

Background: Charging of insulators is a complex phenomenon to simulate since the accuracy of the simulations is very sensitive to the interaction of electrons with matter and electric fields.

Aim: In this study, we report model improvements for a previously developed Monte-Carlo simulator to more accurately simulate samples that charge.

Approach: The improvements include both modeling of low energy electron scattering by first-principle approaches and charging of insulators by the redistribution of the charge carriers in the material with an electron beam-induced conductivity and a dielectric breakdown model.

Results: The first-principle scattering models provide a more realistic charge distribution cloud in the material and a better match between noncharging simulations and experimental results. The improvements on the charging models, which mainly focus on the redistribution of the charge carriers, lead to a smoother distribution of the charges and better experimental agreement of charging simulations.

Conclusions: Combined with a more accurate tracing of low energy electrons in the electric field, we managed to reproduce the dynamically changing charging contrast due to an induced positive surface potential.

© *2019 Society of Photo-Optical Instrumentation Engineers (SPIE)* [DOI: 10.1117/1.JMM.18.4.044003]

Keywords: charging; scanning electron microscope; Monte-Carlo simulation; electron beam-induced conductivity; breakdown; low energy electrons.

Paper 19063 received Jul. 19, 2019; accepted for publication Nov. 18, 2019; published online Dec. 5, 2019.

1 Introduction

Electron beam-based inspection techniques have become a standard, where nanometer resolution imaging is required for state-of-the-art semiconductor devices. However, when nonconductive materials are involved, charging occurs and issues are reported, such as image distortion due to primary beam deflection[1–5] and image contrast changes due to the changing secondary electron (SE) emission.[6–8] As a consequence, measurements of critical dimensions will be less accurate.[9–11] Therefore, a better understanding of the charging effects on electron imaging becomes crucial for metrology.

Several Monte-Carlo studies were reported that included charging effects, but they rather focused on simulations for simplified geometries, such as semi-infinite surfaces.[12–14] Besides that, some Monte-Carlo simulators were developed to simulate full 3D geometries and charging models were also incorporated.[15–19] However, the long calculation times of these simulators render them quite impractical for realistic scenarios.

In an earlier study, we reported a Monte-Carlo simulator that included charging effects, making use of a multigrid-based electric field solver to decrease the electric field computation time.[20] Combining the electric field solver with a semiempirical electron–matter interaction model, we were able to simulate a scanning electron microscope (SEM) image of an area of $\sim 1.5\ \mu\text{m}^2$ of grating couplers, as shown in Fig. 1(a), in about 1 h.[20] However, the shadowing phenomenon (bright-to-dark transition) on the oxide pads, seen in Fig. 1, could not be reproduced in the simulation [Fig. 1(c)]. Including the charging model only led to a blur of the edges due to beam deflection, see Figs. 1(b) and 1(c).

To properly include the charging effects, it is important to accurately model the electron–matter interaction, especially for low energetic electrons, which are very sensitive to the local electric fields. Therefore, improvements are needed for both the electron scattering models and the charging models. In this work, we report our attempts to improve both.

First, we improved the electron scattering models by incorporating discrete scattering of electrons instead of the continuous slowing down approximation (CSDA). Inelastic scattering is modeled using the dielectric function. Also, electron–phonon scattering and quantum mechanical transmission through boundaries are implemented. Moreover, solid-state effects on the atomic potential are taken into account in modeling the elastic scattering. All electrons are traced until their energy is below the surface barrier of $\sim$10 eV, measured with respect to the bottom of the band.

Second, we addressed issues exclusively relevant for insulators, namely charge redistribution to include effects, such as electron beam-induced conductivity (EBIC). The most straightforward approach would be to completely ignore charge redistribution in insulators, as was done in our previous study,[20] or only consider catastrophic effects like dielectric breakdown. The other extreme would be modeling

*Address all correspondence to Kerim T. Arat, E-mail: k.t.arat@tudelft.nl

1932-5150/2019/$28.00 © 2019 SPIE

Downloaded From: https://www.spiedigitallibrary.org/journals/Journal-of-Micro/Nanolithography,-MEMS,-and-MOEMS on 06 Feb 2020
Terms of Use: https://www.spiedigitallibrary.org/terms-of-use

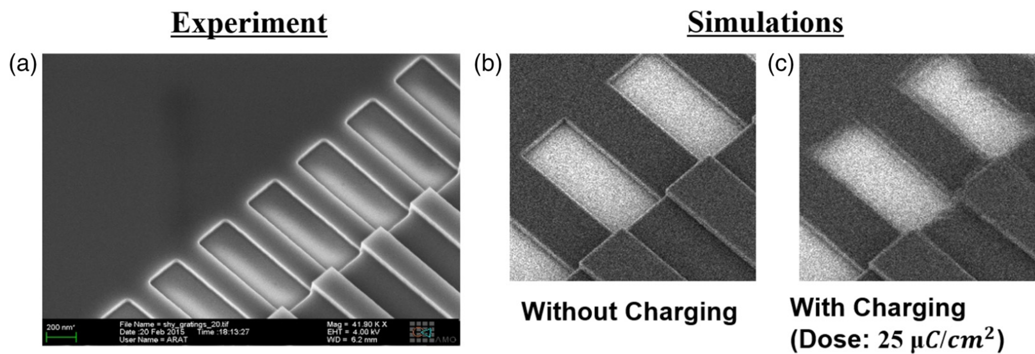

Fig. 1 (a) Experimental SEM image of a grating coupler[20] compared with (b) the simulated image without charging, and (c) the simulated image with charging taken into account. Simulated areas [in panels (b) and (c)] are $1.2 \times 1.2\ \mu m^2$.

from first principles, including effects like electron–hole recombination and trapping. We chose a midway and modeled the charge redistribution effects using phenomenological models with a limited number of calibration parameters.[21]

After that, the effect of charging on the electron emission from a bulk oxide sample during a linescan, for different doses, is demonstrated. Subsequently, a top-down view of the grating couplers is simulated where the charging (bright-to-dark) contrast is present. Finally, the impact of the charge redistribution model is shown on a test sample with four metal contact pads embedded in a thin silicon dioxide (SiO_2) layer on top of a silicon (Si) wafer. Three pads are electrically floating (no contact with the underlying Si wafer), and the fourth one is connected to the underlying Si wafer. The effect on the simulated SEM images is shown when the charging and/or EBIC model is switched on. The models lead to more realistic images and can reproduce phenomena that were not possible to reproduce with the previous models.

2 Scattering Model

We will now first describe the scattering model improvements and assume that the scattering cross-sections do not change due to charging. The electron trajectories are influenced by the charge clouds in the materials, which are formed by electrons getting trapped (negative charge) or electrons generating new electrons (both negative and positive charge). Hence, accurate modeling of electron generation, transport, and boundary-crossing is essential to understand the charge distribution in the material and the electron emission.

In our previous study,[20] the semiempirical scattering models were designed to get an accurate value of the SE yield for a semi-infinite surface. However, an accurate SE yield does not guarantee a realistic scattering cloud inside the material, as shown in Fig. 2(a). The very different scattering cloud will not only affect charge distribution but also the detected signal from topographical structures. It is still possible to generate a more realistic scattering cloud using CSDA, similar to Fig. 2(b), by allowing the generation and scattering of electrons in deeper regions of the material, but any inaccuracy due to the approximate model will lead to a deviation of the charging phenomenon. Therefore, we preferred to use first principle modeling to determine the charge distribution.

2.1 *Improvements on Elastic Scattering Cross-Sections*

In our earlier work, Mott cross-sections were used to calculate the elastic scattering mean free paths and the scattering angles. However, the calculations were done for a "free atom" potential, which is not quite appropriate for our application because solid-state effects are not included. Instead, a "muffin-tin" potential is more realistic. Furthermore, the indistinguishability of the incident electron from the bound electrons, "exchange-correction," and the polarization of the target atom due to incident electrons, "correlation-polarization" are also included. All these options are offered by the ELSEPA package.[22] For Si, the "muffin-tin" potential results in ∼1.5 times larger mean free paths, as shown in Fig. 3. At low energies, below a few hundred electron volts (eV), the Mott cross-sections turn out to become very sensitive to the atomic potential.[23] Because at these low energies (the quasi-elastic), electron–phonon interaction becomes dominant, we followed the approach suggested by Verduin[24] and use the electron–phonon scattering model for low energies. Therefore, in the present study, the elastic scattering cross-section consists of

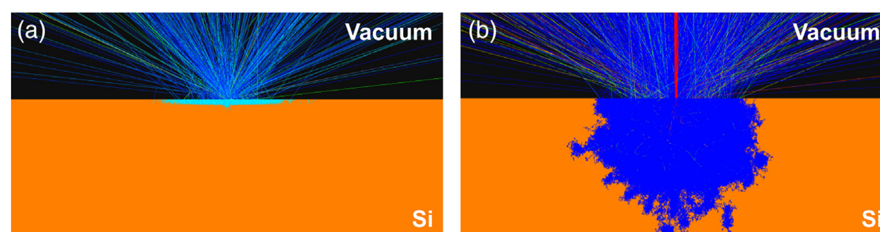

Fig. 2 Scattering cloud of SEs: the generic shape of the cloud obtained with (a) the approximate (former) models and (b) first principle (current) models. In panel (a), only SEs that can escape are generated and in (b), all SEs are generated and traced.

Downloaded From: https://www.spiedigitallibrary.org/journals/Journal-of-Micro/Nanolithography,-MEMS,-and-MOEMS on 06 Feb 2020
Terms of Use: https://www.spiedigitallibrary.org/terms-of-use

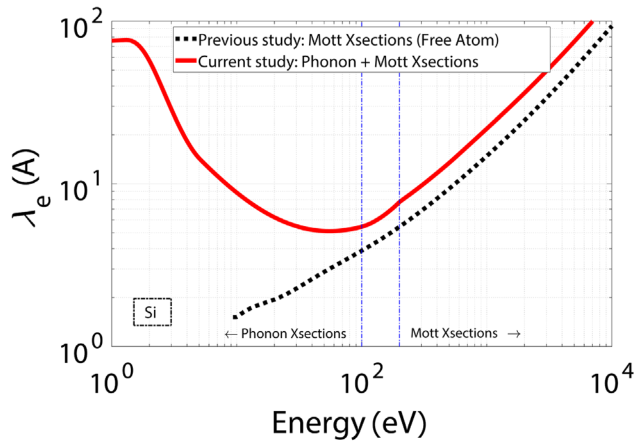

Fig. 3 Elastic mean free path versus energy for Si: it consists of an interpolation between the Mott cross-section (energy > 200 eV) and phonon cross-sections (energy < 100 eV). The Mott cross-sections were calculated by ELSEPA,[22] assuming the muffin-tin approximation, exchange correction, and correlation-polarization effects.

- Mott cross-section (muffin-tin + "exchange correction" + "correlation-polarization") for energy > 200 eV
- Acoustic phonon scattering cross-section for energy <100 eV.

For energies between 100 and 200 eV, the cross-section is interpolated between the two.

Material parameters, especially related to acoustic phonons, are not easy to find. To serve the interested reader, we list the parameters used in this work in Table 1.

Density ρ_m, Fermi energy E_F, work function W, electron affinity χ, bandgap E_g at 300 K, density of state mass m_{dos}, effective mass of electron m_{eff}, screening parameter A_{ac}, speed of sound in solid u_s, and acoustic deformation potential ε_{ac} are given in Table 1. [*] are calculated values and [+] are assumed values. The net-average energy loss in the phonon scattering, E_{Ph}, is calculated by Eq. (3.116) in Ref. 24.

Table 1 Material parameters for Si, Cu, and SiO_2.

		Si	Cu	SiO_2
ρ_m (g/cm^3)		2.329[25]	8.96[26]	2.648[27]
E_F (eV)		7.83	7.0[28]	—
W or χ (eV)		4.05	4.65[28]	0.9[29]
E_g (eV)		1.12	—	9.0[29]
m_{dos} (m_e)		1.08[30]	1.0[24]	1.0[+]
m_{eff} (m_e)		0.26[30]	1.01[28]	1.0[+]
A_{ac}		5[+]	5[+]	7[31]
E_{Ph} (meV)		14[*]	12.6[*]	6.8[*]
u_s (m/s)	Longitudinal	9130[32]	4760[28]	3560[31]
	Transversal	5842[32]	2325[28]	3560[+]
ε_{ac} (eV)	Longitudinal	9.2[33]	4.76[*]	3.4[31]
	Transversal	5.0[33]	3.72[*]	3.4[+]

2.2 *Improvements on Inelastic Scattering Cross-Sections*

In the previous study,[20] an algorithm based on CSDA was used to model the energy transfer of the primary electrons.[34] Although CSDA is a good approximation to estimate stopping power (SP) at high energies, it overestimates the SP at very low energies. Furthermore, it does not describe the SE generation. Therefore, we have employed the first principle modeling to simulate the low energetic electrons as accurately as possible. In this study, energy and momentum transfer of an electron to the material is modeled by the dielectric function formalism using optical data.[35] It allows the calculation of inelastic events discretely, as depicted in Fig. 4.

To calculate inelastic cross-sections, we take Ashley's (simple) model[35] and adopted the refinements suggested by Kieft and Bosch,[23] i.e., no exchange correction for energies <50 eV, and restrict energy losses, such that electrons cannot end up with an energy lower than the Fermi level. We have used the density per atom for elements, such as Si and copper (Cu), and the density per molecule for molecules and compounds, such as SiO_2, when calculating the mean free paths.

The SP from the previous study is compared to the powers, as obtained from the refined Ashley model for Si in Fig. 5(a). It is seen to be identical for energies above 1 keV but deviates at lower energies. The elastic and inelastic mean free paths are also given in Fig. 5(b).

We obtain the energy transfer using the dielectric function formalism. This, however, does not provide the initial (binding) energy of the SE prior to a scattering event. We model that following the approach suggested by Kieft and Bosch.[23]

For insulators like SiO_2, electron trapping due to polaronic effects has been reported by several authors,[12,36,37] but none of them is based on a first principle physics model. In this study, the nominal SE emission is unrealistically high (7 at its maximum) without explicit implementation of trapping cross-sections (Fig. 6). Therefore, we also implemented an empirical model[12] for trapping cross-sections for SiO_2 to not neglect the trapping phenomenon in insulators and to lower the nominal (theoretical) SE yield to values in agreement with those reported by Schreiber and Fitting[31] and Ohya et al.[36] We have used $S_{trap} = 0.2$ (1/nm) and $\gamma_{trap} = 0.2$ (1/eV) when calculating the trapping cross-sections from Eq. (13) of Ref. 12. The SE and backscattered electron (BSE) yields of SiO_2 with and without trapping cross-sections are given in Fig. 6. The inclusion of the trapping cross-sections hardly affects the BSE yield because trapping only has an effect on very slow electrons.

2.3 *Improvements on Boundary Crossing*

The lower the electron energy, the more its path is affected when it interacts with a boundary and as a result, it can be reflected or transmitted. Modeling the boundary-crossing correctly is crucial for SE emission. In the previous study, the probability of crossing the surface barrier was modeled using momentum conservation only. That is, if the electron approaches the surface under an angle bigger than the critical

Downloaded From: https://www.spiedigitallibrary.org/journals/Journal-of-Micro/Nanolithography,-MEMS,-and-MOEMS on 06 Feb 2020
Terms of Use: https://www.spiedigitallibrary.org/terms-of-use

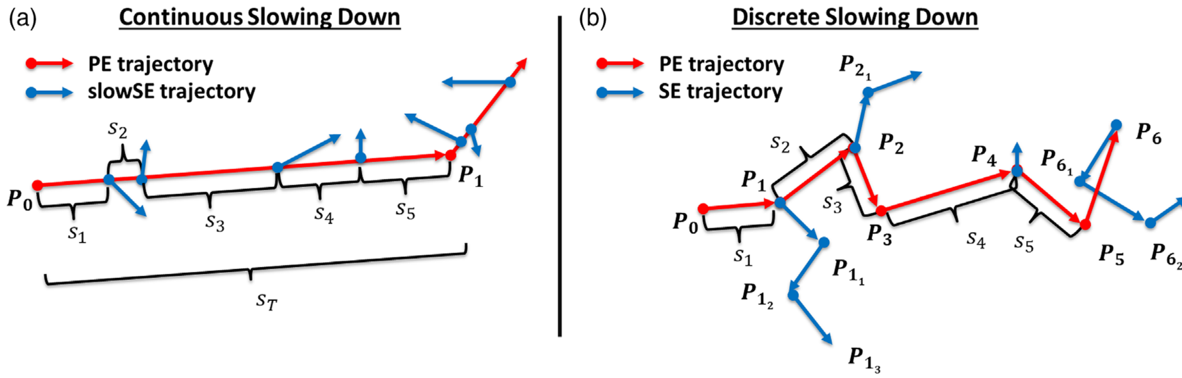

Fig. 4 Inelastic scattering: (a) a semiempirical model is used in the previous study, which is based on the CSDA. It estimates the number of (slow) SEs and their energies for a path length (ST) from the stopping power; (b) first principle modeling is used in the current study, which is based on dielectric function formalism. It estimates the inelastic mean free path, energy and momentum transfer for each inelastic event (P1, P2, P4, and P6) based on the energy loss function.

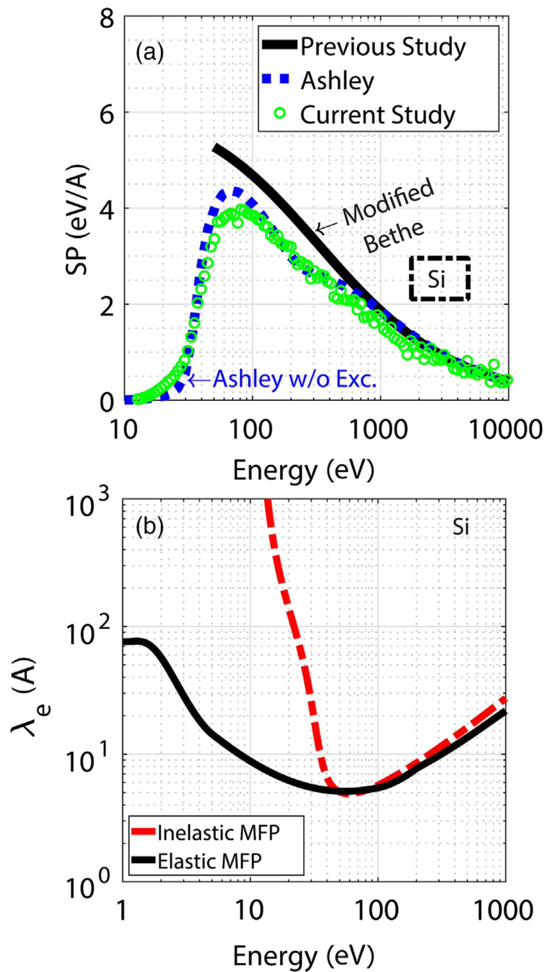

Fig. 5 Modelling inelastic scattering: (a) stopping power and (b) comparison of mean free paths of Si in the current study.

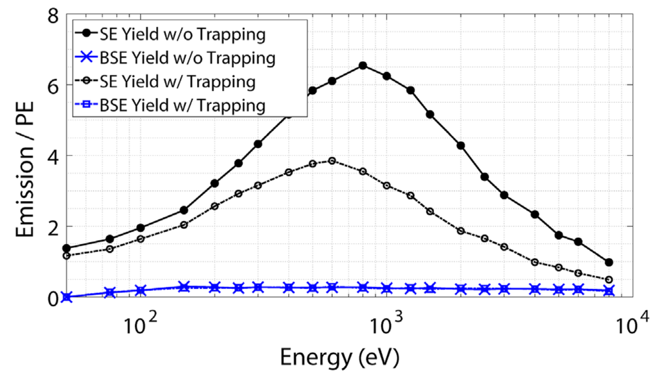

Fig. 6 Comparison of emission yields with (w/) and with (w/o) trapping cross-sections.

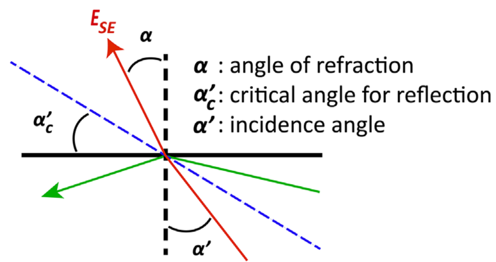

Fig. 7 Transmission of an electron from the surface.

angle (α_c', see Fig. 7), then it will be reflected (total internal reflection).

In this study, the probability of transmission is determined quantum mechanically.[38] When the electron is considered as a wave, there is a probability that part of the wave is transmitted through the boundary and part of it is reflected. Equation (1) gives the probability of transmission for an electron:

$$P(\alpha') = \frac{4\sqrt{1 + \frac{-\Delta U}{E\cos^2\alpha'}}}{\left(1 + \sqrt{1 + \frac{-\Delta U}{E\cos^2\alpha'}}\right)^2}, \tag{1}$$

where ΔU is the net change in kinetic energy, E is the kinetic energy of the electron, and α' is the angle of incidence.

3 Charging Model

The basic principle of the Monte-Carlo simulation of the interaction of individual electrons and the continuously

Downloaded From: https://www.spiedigitallibrary.org/journals/Journal-of-Micro/Nanolithography,-MEMS,-and-MOEMS on 06 Feb 2020
Terms of Use: https://www.spiedigitallibrary.org/terms-of-use

changing electric fields and accompanying charging effects is simple: a certain number of PEs is simulated, and then, the field solver updates the field and redistributes the charge as needed. This procedure is repeated many times, typically at least once per simulated pixel. Updating multiple times for a single pixel is not unreasonable either, say after every 200 PEs. The detailed-level interaction between the field solver, the Monte-Carlo simulation, and the charge redistribution models is more complicated. The numerical discontinuities of the electric field solution must be handled by the Monte-Carlo simulation, and the charge redistribution models tend to make the solution of the field equation more difficult and time-consuming.

3.1 *Electric Field Solver*

The electric field solver uses the Poisson equation:

$$-\nabla \cdot [\epsilon_r(r)\nabla V(r)] = \frac{\rho(r)}{\epsilon_0}, \tag{2}$$

in which $\rho(r)$ is the charge distribution, $V(r)$ is the potential, $\epsilon_r(r)$ is the dielectric constant of the material, and ϵ_0 is the permittivity in a vacuum. It is used with the constitutive material equation [Eq. (3)]:

$$J = -\sigma\nabla V \tag{3}$$

and the continuity equation [Eq. (4)]:

$$\frac{\partial\rho}{\partial t} + \nabla \cdot J = 0, \tag{4}$$

in which J is the current density and σ is the conductivity. This equation [Eq. (4)] is solved by an implicit Euler scheme:

$$\frac{\rho_n - \rho_{n-1}}{\Delta \mathrm{t}} = \nabla \cdot (\sigma\nabla V_n), \tag{5}$$

where V_n is determined by

$$\frac{\rho_n}{\epsilon_0} = -\nabla \cdot (\epsilon_r\nabla V_n) = \frac{\rho_{n-1}}{\epsilon_0} + \frac{\Delta \mathrm{t}}{\epsilon_0}\nabla \cdot (\sigma\nabla V_n), \tag{6}$$

giving a Poisson equation with modified material parameters:

$$-\nabla \cdot \left[\left(\epsilon_r(r) + \frac{\Delta \mathrm{t}}{\epsilon_0}\sigma(\mathrm{r},\mathrm{t})\right)\nabla V_n\right] = \frac{\rho_{n-1}}{\epsilon_0}. \tag{7}$$

The charges deposited during the time step by the Monte-Carlo simulation are added to ρ_{n-1} before this equation [Eq. (7)] is solved, which works if we only make a single-time step between Monte-Carlo simulations.

The conductivity $\sigma(r, t)$ in this equation depends on space and time because we include charge redistribution effects by an induced conductivity model. The conductivity also depends on the electric field strength because we include a dielectric breakdown model. However, this dependency is suppressed here because the main numerical effort for the solution of the equation is as if the conductivity would be a fixed known function of space and time. (A more physical model would include the dependency of the conductivity on the electron and hole concentrations, but this dependency cannot be suppressed and the numerical solution of the resulting equations would be challenging.)

The modified equation is harder to solve than the original equation since $\sigma(r, t)$ normally changes quickly in both space and time. We previously had the option to use a direct solver as a slow but robust and accurate reference solver. This is no longer possible since the expensive initial factorization must be repeated for each time step. Therefore, we integrated a modern algebraic multigrid solver, namely Daniel A. Spielman's modified implementation of Kyng and Sachdeva.[39] It was initially more than a factor 3 slower than the existing multigrid solver, but a C++ port and tighter integration reduced that factor to 1.5. It was later used to enable more flexible meshing, which turned out to save a factor 2 to 3 (and possibly more) for certain use cases. The C++ port has been parallelized, but parallel scaling is limited. The best speedup is achieved with four threads, but it is only slightly above a factor 2. The existing multigrid solver has also been parallelized. The best speedup is still achieved with four threads, but the scaling is better. This solver is used when explicit simulation times are reported.

The modified equation also affects the geometric multigrid solver. It becomes less robust because the material parameters are changing quickly on a very small spatial scale. We improved robustness by using a preconditioned conjugate gradient method, where the multigrid solver acts as a preconditioner. We also tried (and failed) to use another Krylov method, namely replacing the W-cycle by the K-cycle introduced by Notay and Vassilevski[40] for algebraic multigrid methods (AMG). However, what really improved the robustness significantly was to use locally either the continuity equation or the Poisson equation as they occur in Eq. (5) to update the charge distribution, depending on which is locally less affected by inaccuracies in the potential.

3.2 *Tracing Electrons*

The electrons both in the sample and in vacuum are traced subject to the influence of the current electric field. The numerically solved electric field is discontinuous at cell boundaries since the finite-element method is used for discretization of the field equations. At material interfaces, the normal component of the electric field is discontinuous even for the exact solution. This severely limits the choice of reasonable integration methods. The velocity Verlet scheme is used because it leads to (piecewise) parabolic trajectories, for which it is easy to exactly compute the intersections with the mesh of the field solver (or the geometry). The velocity Verlet scheme approximates the equation:

$$\ddot{x}(t) = a[x(t)] \tag{8}$$

as

$$x(t + \Delta t) = x(t) + v(t)\Delta t + \frac{1}{2}a\Delta t^2, \tag{9}$$

$$v(t + \Delta t) = v(t) + \frac{a(t) + a(t + \Delta t)}{2}\Delta t. \tag{10}$$

This scheme is applied with respect to time, but the simulation needs the trajectory for a given distance. If the distance along the trajectory to the next intersection with an interface is shorter than the given distance, then the

Downloaded From: https://www.spiedigitallibrary.org/journals/Journal-of-Micro/Nanolithography,-MEMS,-and-MOEMS on 06 Feb 2020
Terms of Use: https://www.spiedigitallibrary.org/terms-of-use

corresponding time step Δt can be determined exactly. If not, then Δt is determined from a given distance Δs via $\Delta t = \frac{\Delta s}{|v|}$. In theory, this inaccurate value for the time step seems to reduce the accuracy of the method. However, in practice, either the electron is inside a material and Δs is very small, or the electron is in vacuum and Δs is big but irrelevant.

3.3 *Modeling of Sample Charging*

The basis for sample charging is that the creation of a SE deposits a positive charge and stopping an electron deposits a negative charge. At room temperature, both positive holes and negative electrons would continue to move and also drift in local electric fields, but modeling the movements of individual holes and electrons with thermal energy is not practical. We implemented macroscopic models for induced conductivity, dielectric breakdown, and charge diffusion. We will ignore the charge diffusion model since we did not use it for the simulations presented later and do not have sufficient intuition of how to set its model parameters. The motivation, modeling, and implementation of the other two models are described in the following sections.

3.4 *Induced Conductivity*

Slow electrons returning from the vacuum back to the sample tend to accumulate very close to the sample surface. The surface then tends to charge negatively and develop a dipole layer, at least in the simulation. It is not clear whether there are physical effects, which could neutralize that dipole layer completely within a short time. One main charge redistribution effect is that the beam generates free holes and electrons, which locally turn insulators into conductors. This also counters dipole layer formation, so it would be nice if this charge redistribution effect could be included in the simulation.

To avoid the complicated physics of electron and hole transport, recombination and trapping, as a first step, an established empirical quasistatic electron beam-induced conductivity model is attractive. Induced conductivity, in general, occurs due to the local ionization of the material as long as free electrons or holes are locally present, i.e., the material is locally conductive. This will allow some surface conductivity as long as there is a charge imbalance due to recollected slow electrons by a positive surface potential. More specifically, the implemented model expresses the conductivity using the deposited energy (in Gray) per kilogram per time $D(r, t)$ as follows:

$$\sigma(r, t) = k \cdot D(r, t)^{\Delta}, \tag{11}$$

where we used $k = 10^{-14}\ \mathrm{S/m(Gy/s)}^{\Delta}$ (EBIC constant) and $\Delta = 1.0$ (EBIC exponent) for SiO_2 in the simulation. This model assumes a slowly changing (quasi-static) deposited energy per time. However, we use it (incorrectly) for the quick scanning and a finely resolved grid with very few electrons. Still, it allows studying the impact of this sort of charge redistribution effect and how it reduces the undesired dipole layer near the sample surface. Here, the deposited energy includes the energy lost in a scattering event and energy of trapped electrons.

In Ref. 21, this model is used correctly for a defocused (quasi-static) beam with $k = 7.7 \times 10^{-18}\ \mathrm{s}^{\Delta}/(\Omega \cdot \mathrm{cm} \cdot \mathrm{rad}^{\Delta})$ and $\Delta = 0.89$ for a red polymethyl methacrylate (PMMA), as given by Tanaka et al.[41] To convert this to SI units, one has to multiply by $100 \times 100^{\Delta}$, giving $k = 4.6 \times 10^{-14}\ \mathrm{S/m}\ (\mathrm{Gy/s})^{\Delta}$.

3.5 *Dielectric Breakdown*

Even with an empirical EBIC model, as described in the previous section, one can still sometimes observe unphysically huge electric field strengths. So, it makes sense to include a dielectric breakdown model as a fallback for those cases, where the electric field strength grows huge. That can be caused by simulation artifacts like a missing physical effect, or it can be a real physical effect, for example, if two conductors are separated by a very thin insulating layer.

Instead of modeling the detailed generation of electron–hole pairs in an avalanche breakdown event, it is assumed that an isolated material will become perfectly conducting locally at the places, where the field strength exceeds the dielectric strength of the material. During a breakdown event, the region where an insulator becomes conducting can travel (or grow) through space, as long as the underlying charge distribution is not sufficiently neutralized.

The model is implemented by setting the cells where the field strength currently exceeds a given threshold to perfectly conducting. Next, the field is computed again, the charges are redistributed accordingly, and then further perfectly conducting cells are added, where the new field exceeds the threshold. This procedure is repeated until either the field no longer exceeds the threshold anywhere, or after the procedure was repeated a predefined number of times. The perfectly conducting region grows during the simulation of the breakdown event, but after it is finished, the previous material properties are used again, as if the breakdown would not have harmed the isolator at all. Hence, it makes sense to remember any cell that temporarily got affected by breakdown (and the maximal field strength by which it got affected) for later inspection.

Although not based on first-principle physics, having a robust breakdown model, as described above, is important to prevent simulations from failing due to huge electric field strengths. It is unclear to what extent other simulators also rely on that. Grella et al.[42] wrote: "Breakdown effects are taken into account by limiting the field in the sample" and Shadman and De[43] say about the same simulator: "Still, the amount of charge that these currents deposit can potentially raise the electric field in a dielectric to induce a current. Makeshift conductivity models have been implemented to address the resulting redistribution of the embedded charge." Even the Java source code of JMONSEL includes a breakdown model, which was the initial motivation to investigate this sort of model.

4 Results

4.1 *Effect of New Scattering Models—No-Charge Up Scenarios*

In Fig. 2, the scattering clouds of the electrons were shown. The different forms of clouds will not only make a difference in the charge distribution profile in the material but also on the emission, especially for topographic structures. Therefore, we first test the effect of the improvements independent of the charging models on a topographic surface.

Downloaded From: https://www.spiedigitallibrary.org/journals/Journal-of-Micro/Nanolithography,-MEMS,-and-MOEMS on 06 Feb 2020
Terms of Use: https://www.spiedigitallibrary.org/terms-of-use

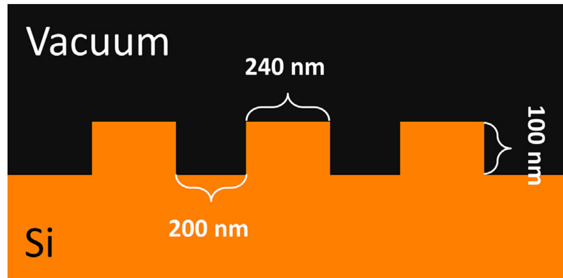

Fig. 8 The cross-section view of an RM 8820 sample used to simulate. The line width is 240 nm and the height is 100 nm. The spacing is 200 nm.

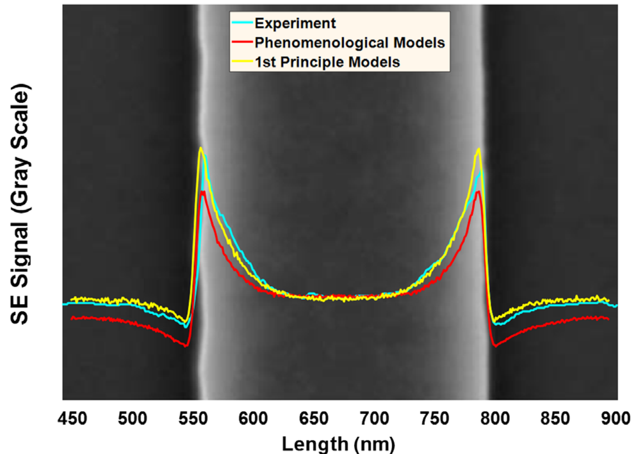

Fig. 9 SE signal from a silicon line on top of a silicon surface, and an experimental line scan, a line scan simulated using our previous phenomenological models, and a line scan simulated with the present first principle models.

We simulated 200-nm pitch patterns from RM 8820 samples, which were introduced by NIST as a test and calibration standard for scanning probe microscopy.[44,45] They consist of amorphous silicon lines deposited on top of a silicon substrate. In Fig. 8, the cross-section view of the simulated lines is given.

The experimental results are obtained from a publication.[46] Figure 9 shows a comparison of an experimental line scan with line scans simulated using the phenomenological models from the previous study and using the first principle models introduced in this study. It is assumed that the detection efficiency is best at the top of the silicon line. Hence, the signals were aligned such that the intensities there coincide. The agreement between the experiment and the first principle model simulation used in this study is better than the simulation of the previous study.

4.2 *Effect of Model Improvements on SE Emission*

In theory, when the primary energy is in between the crossover energies E_1 and E_2, as shown in Fig. 10, the total electron emission from the sample surface is more than the incident primary current ($I/I_p > 1$). Therefore, it is expected that a dielectric material gets positively charged. However, it is reported that the positive charging process is self-regulatory[3,7,47] due to the recollection of the electrons by the sample. Therefore, the total yield (SE + BSE) becomes ∼1.

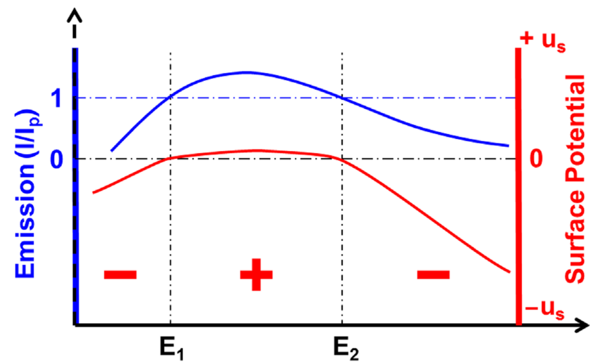

Fig. 10 The surface potential of insulators during the charging process.

The "nominal" SE yield, i.e., the yield ignoring all charging, from SiO_2 is ∼7 at 1 keV. In a more realistic scenario, when scanning the primary beam across the sample, the expectation is that the SE yield drops along the scan line due to the positive surface potential, i.e., a drop in the signal is observed. Therefore, we tested whether the simulator produces the described phenomenon.

The first two steps of a line scan on bulk material are shown in Fig. 11. The scan area is 100 nm and the pixel size is 2.5 nm. The beam energy and spot size are 1 keV and 3 nm (full width half maximum), respectively. The dose is 250 $\mu C/cm^2$ (100 electrons/pixel) and the electric field is updated for every pixel with the AMG solver. The beam current is 100 pA. The breakdown module is enabled with a threshold value of 50 MV/m.[48]

Until the first computation of the electric field, the SiO_2 sample stays neutral and all of the emitted electrons reach the detector above the sample [Fig. 11(a)]. After the field is computed from the charge distribution obtained from the previous scattering events [inset Fig. 11(a)], electrons start to experience the positive potential at the surface and the electrons with energy less than the surface potential return to the sample [Fig. 11(b), the inset shows the field and the returning electron trajectories]. It is observed that the (maximum) potential increases, 0 V, 3.47 V, 5.6 V, etc., for the first couple of pixels and then saturates around ∼11 V. The effect of the charging on the emission is shown in Fig. 12(a). As expected, the total emission is high for the first couple of pixels, then decreases and saturates after ∼25 nm (10 pixels). Note that the frequency of the field update has an impact on the emission especially for the first couple of pixels. The sensitivity of the results will be discussed in Sec. 5. The stable BSE emission indicates that the surface potential stays rather small, affecting only the low energetic SEs.

When the dose is decreased to 25 $\mu C/cm^2$ (10 electrons/pixel), the number of created charge carriers per voxel is less. Therefore, the magnitude of the local field becomes smaller than at a higher dose and more electrons will reach the detector. In Fig. 12(b), the corresponding signal drop saturates after about 100 nm, which causes a larger bright-to-dark transition area on the SEM image. The increased noise in the signal is due to shot noise, being larger for a lower amount of electrons in the probe. Similar behavior, but with smaller slopes, is observed when the trapping cross-sections are enabled. Figures 12(c) and 12(d) show that in case the emission is not very high, the charging effect can be subtle.

Downloaded From: https://www.spiedigitallibrary.org/journals/Journal-of-Micro/Nanolithography,-MEMS,-and-MOEMS on 06 Feb 2020
Terms of Use: https://www.spiedigitallibrary.org/terms-of-use

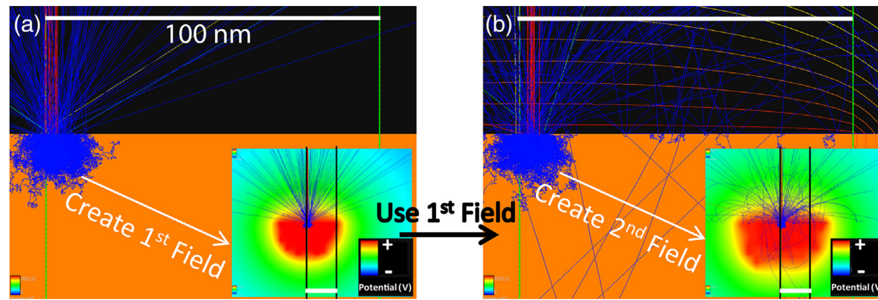

Fig. 11 Charging simulation of a line scan: the initial two steps are depicted. At the beginning (a) big view, there is no field. Hence, the trajectories (red for high energy; blue for low energy electrons) are straight. After the scattering is completed, the electric field is calculated with the distributed charges in the material [the inset in (a), note that the scale is different from the big view image]. The simulator uses the computed e-field to trace the electrons at the next beam position. (b) Isolines indicate the presence of fields in big view. Similarly, the electric field is computed for the next beam in the linescan. As the SEs are recollected by the positive surface potential [the inset in (b)], the SE signal decreases. Scale bars are 100 nm, which indicate the scan area.

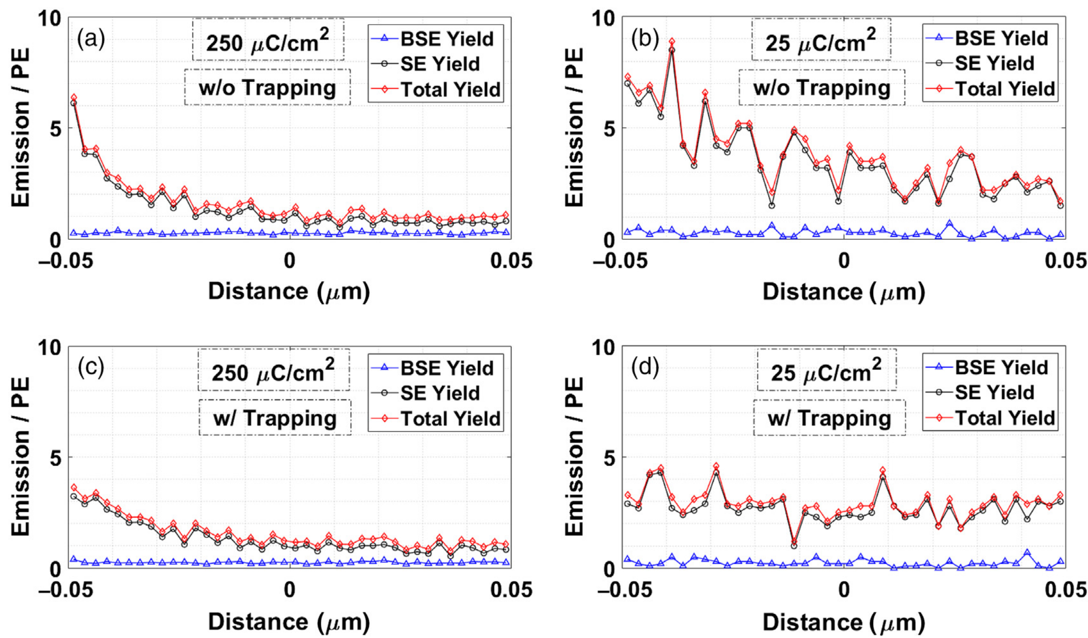

Fig. 12 The effect of dose on electron emission: (a, c) the dose is 250 μC/cm^2; (b, d) the dose is 25 μC/cm^2. For (a) and (b), trapping cross-sections are not used; and for (c) and (d), trapping cross-sections are used. Beam energy is 1 keV.

The results show that the simulations are sensitive to parameters affecting the charge carrier density, such as the dose. This can lead to different results in measurements with dielectrics, where contrast is playing a role.

4.3 *Effect of Model Improvements on the Grating Coupler Simulations*

In the previous study,[20] the grating coupler is described in detail. In Fig. 13(a), a top-down view of the device is shown. Figure 13(b) shows a zoomed-in image of the second trench, and Fig. 13(c) shows the intensity profile across the middle of that trench. Note that the scan direction is from left-to-right (fast-scan axis) and top-to-bottom (slow-scan axis). The topographic contrast is visible on the surrounding silicon structures and also on the oxide inside the trenches. In addition, there is an extra contrast in the trenches along the fast-scan direction, which is asymmetric in the intensity profile. That is, the peak intensity along the x axis is positioned left from the center of the trench. This can be explained as follows. The electron probe visits the left side of the oxide in the trench first and creates a positive surface potential. As it visits the next pixels of the scanline, the surface potential slightly accumulates and causes a decreasing SE signal at those pixels. The phenomenon qualitatively agrees with the theory described in Sec. 4.2.

When simulating these trenches, including charging, a similar bright-to-dark contrast, as discussed above, is observed (see Fig. 14). It does show the asymmetry in the contrast across the trench, which could not be achieved in our previous work, but the asymmetry is much larger than observed in Fig. 13. We also clearly see the effect of EBIC in Fig. 14, the signal increasing toward the edges of the trenches. We then included trapping cross-sections, which leads to a lower nominal yield and thus a smaller positive

Downloaded From: https://www.spiedigitallibrary.org/journals/Journal-of-Micro/Nanolithography,-MEMS,-and-MOEMS on 06 Feb 2020
Terms of Use: https://www.spiedigitallibrary.org/terms-of-use

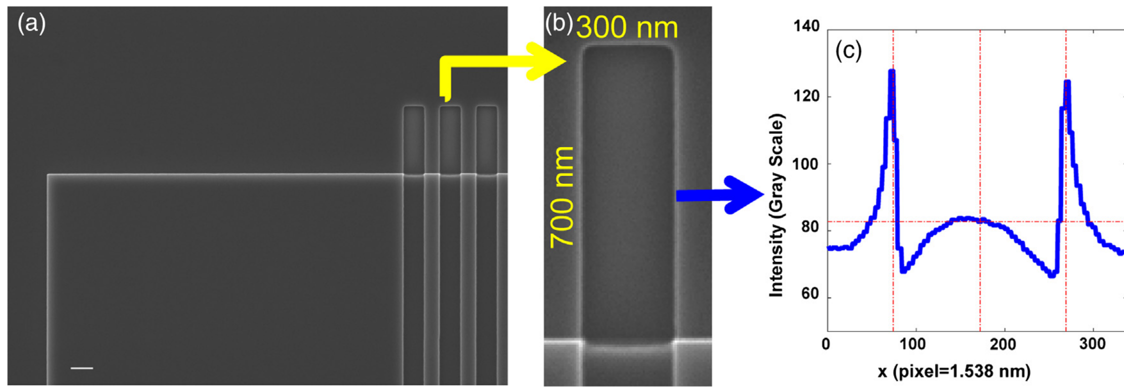

Fig. 13 Experimental SEM image of a grating coupler is taken at 4 keV. (a) Top-down view of the vertical lines (scale bar: 300 nm), (b) zoomed-in view of the second trench (scale bar: 100 nm), and (c) SE signal profile of the middle image, integrated over 10 pixels along the y axis.

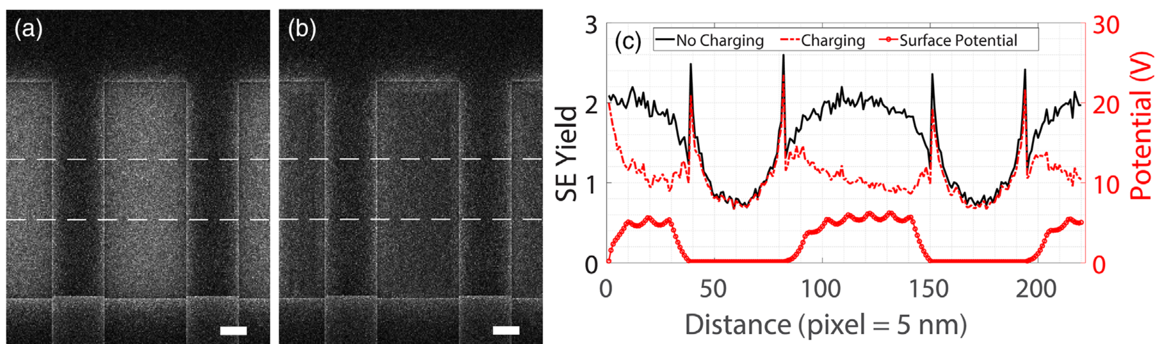

Fig. 14 Trenches of the grating coupler simulated with first principle scattering models. (a) Image simulated without charging models; (b) image simulated with charging models; (c) SE signal profile of the panels (a) and (b) was integrated and averaged over 50 pixels along the y axis (between the dashed lines in a and b). The right y axis is for the surface potential value at the incident pixel after the interaction. Scale bars are 100 nm.

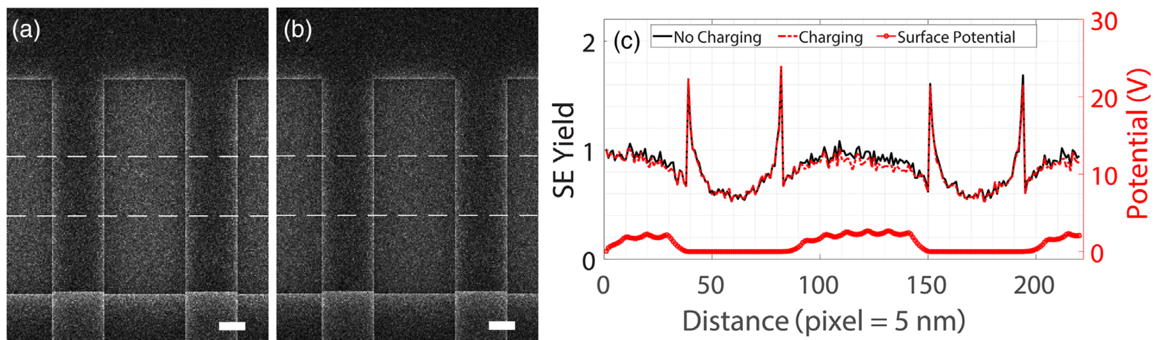

Fig. 15 Simulated trenches of the grating couplers with first principle scattering models and a trapping model included. (a) Image simulated without charging models but with trapping; (b) image simulated with charging and trapping models; (c) SE signal profile of the figures (a) and (b), integrated and averaged over 50 pixels along the y axis [between the dashed lines in (a) and (b)]. The right y axis is for the surface potential value at the incident pixel after the interaction. Note the asymmetric signal (the red dashed curve) in the central trench and the signal suppression in the right half of the trench. Scale bars are 100 nm.

surface potential. The results are shown in Fig. 15. When charging and trapping models are included, the asymmetry in contrast across the trench is clearly seen (the red dotted curve), compared to the case with trapping but without charging (the black solid curve). The positive surface potential due to the charging suppresses the emission from the middle of the trench toward the edge, where the EBIC effect comes into play. To quantify the asymmetric contrast in the simulated trench, the displacement of the maximum contrast in the trench from the middle of the trench is determined as 15 nm. This compares to the experimentally determined displacement, from Fig. 13(c) of 17 nm. And comparing the ratio of the areas under the SE signal profile left and right of the middle of the trench, in the experiment, a ratio of 1.17

Downloaded From: https://www.spiedigitallibrary.org/journals/Journal-of-Micro/Nanolithography,-MEMS,-and-MOEMS on 06 Feb 2020
Terms of Use: https://www.spiedigitallibrary.org/terms-of-use

is found, in the simulation with charging a value of 1.187, and in the simulation without charging a value of 1.05. The deviation from 1.00 is due to the noise. The areas were determined with respect to the baseline connecting the lowest intensity points at the edges of the trench. The agreement between experiment and simulation supports our reasoning above that the positive surface potential slowly builds up when scanning over a trench and it indicates that the experimental emission yield is slightly higher than unity at 4 keV, as was assumed in the simulations with scattering models and trapping. We have noticed that, close to the edges of the trench, there is no strong charging effect because of the EBIC effect, and this also agrees well with the experimental observations. The trapping cross-sections allowed us to tune the nominal yield such that it is more comparable to the one reported in Fig. 13 (page 36) by Schreiber and Fitting.[31]

In this simulation, the region of interest is about $\sim 1.5\ \mu\mathrm{m}^2$ ($1.1\ \mu\mathrm{m} \times 1.5\ \mu\mathrm{m}$). The pixel size is 5 nm, and the charging dose is $25\ \mu\mathrm{C/cm}^2$ (40 electrons/pixel). The simulation without charging took 30 min and 44 s on a 64-core workstation. When the trapping cross-section is enabled, the simulation takes 13 min and 50 s. The simulations with charging took 5 h and 19 min and 4 h 20 min on a 32-core workstation without and with trapping, respectively, with Monte-Carlo parallelization (32 threads) and parallelization of the field solver (4 threads).

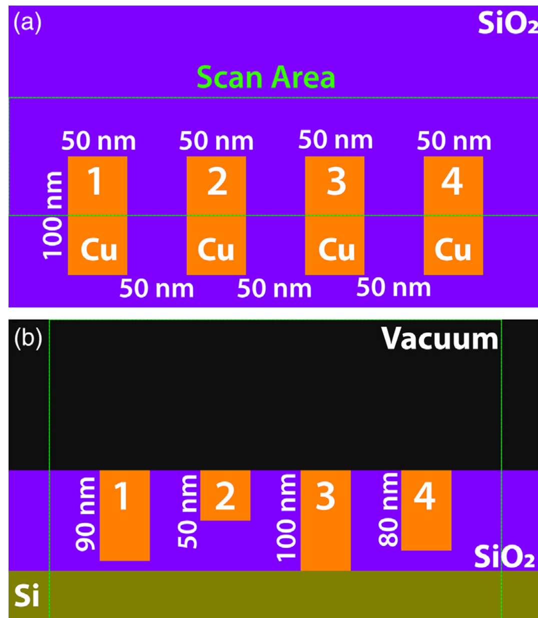

Fig. 16 Sketch of the geometry of the four copper pads: (a) a top-down and (b) a cross-section view. The green lines correspond to the imaging area.

4.4 *Effect of the EBIC Model*

We now show the impact of the charge redistribution model on Cu pads embedded in a thin SiO_2 layer on top of a Si wafer. The pads 1, 2, and 4 are electrically floating (no contact to the underlying Si wafer), and pad number 3 is connected to the underlying Si wafer (see Fig. 16).

In Fig. 17, the effect on the simulated SEM images is shown when the charging model and/or EBIC model is switched on. When the charging model and the EBIC model are switched-off, the copper contacts appear darker in Fig. 17(b) due to their lower SE yield compared to SiO_2 at 0.75 keV (with $128\ \mu\mathrm{C/cm}^2$ charging dose—800 electrons per $10\ \mathrm{nm} \times 10\ \mathrm{nm}$ pixel). Furthermore, the conductive pad (3) is indistinguishable from the others. When the charging model is switched on, but the EBIC and breakdown models are off, the emission of the oxide gets lower due to the positive, surface potential and the SE yield becomes comparable to that of the copper contacts [Fig. 17(c)]. Note that the

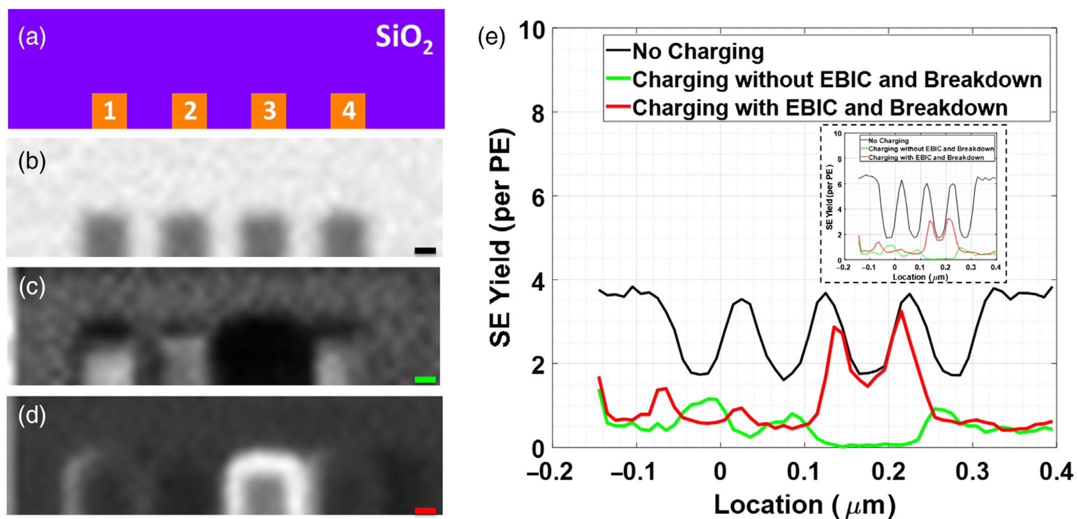

Fig. 17 SEM image simulation of the buried copper pads in Fig. 16. (a) The schematic overview of the pads, (b) charging, EBIC, and breakdown models are switched-off; (c) charging is switched-on but EBIC and breakdown models are off, (d) charging, EBIC, and breakdown models are switched on. The intensity profiles in (e) are obtained at the position of the scale bars (25 nm) in the images (b), (c), and (d). The inset shows the same profiles but without trapping cross-sections. At 0.75 keV, positive charges on the surface retract secondary electrons and the signal intensity decreases. However, the electrically connected copper pad stays neutral, the surrounding area of the pad shows conduction due to EBIC, and the SE yield does not decrease that much (the red and black curves even partly overlap).

Downloaded From: https://www.spiedigitallibrary.org/journals/Journal-of-Micro/Nanolithography,-MEMS,-and-MOEMS on 06 Feb 2020
Terms of Use: https://www.spiedigitallibrary.org/terms-of-use

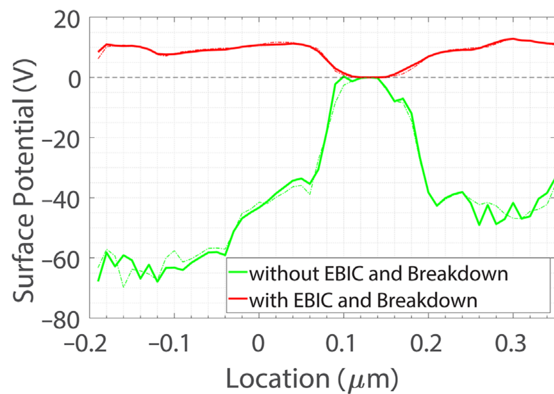

Fig. 18 Surface potential at the pixels after the exposure, where the displayed yields in Fig. 17 are taken. The solid lines are without trapping cross-sections and the dotted lines are with trapping cross-sections.

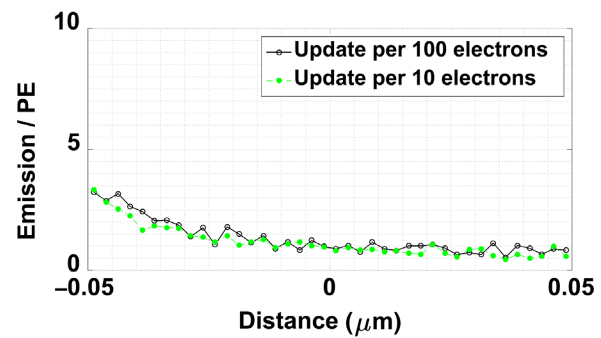

Fig. 19 The effect of electric field update frequency on the results in Fig. 12(c). The solid black line with circles shows when the electric field is updated per 100 electrons (=1 time/pixel); the dashed green line with dots shows when the electric field is updated per 10 electrons (=10 times/pixel).

conductive pad appears different compared to the other pads because conductivity allows it to conduct charge carriers to ground. Switching on the EBIC model, however, leads to more realistic images of the contact pads and the surrounding insulating areas. When the EBIC and the breakdown models are switched-on, the oxide region surrounding the conductive pad experiences induced conductivity and charge carriers are conducted to ground and no charging occurs [Fig. 17(d)]. As a result, the oxide shows the nominal SE yield and becomes brighter than other features.

Figure 17(e) shows the linescan signals across the copper pads. The results in the main graph are simulated with trapping cross-sections and those in the inset without. In contrast to Sec. 4.3, the trapping has a minor influence on the results obtained with the charging models included. The reason is that the high dose that was applied causes the positive surface potential to increase rapidly, right after the starting point of the exposure. This quickly lowers the SE yield to values below one, as is seen by the steep drop of the red and green curves on the left-hand side of Fig. 17(e). For the remainder of the scan, the charge remains more or less in equilibrium.

Figure 18 shows the surface potential of the sample for pixels, where the SE yields are given in Fig. 17(e). The results are given with the same color code (see color online version). For the simulations where EBIC and breakdown models are off, the surface potential is mostly negative except at the copper pad number 3, because it is grounded.

5 Discussion

The frequency of the electric field update is a model parameter. Typically, these fields are updated after a particular number of primaries have completed their interaction with the sample, assuming that the charge accumulation is not significant. In some cases where the emission is very high, like in Fig. 12, the sample can stay uncharged for an unrealistically long time, which can cause an artifact on the emission yield in the first few pixels. However, once the e-field is updated as the simulation proceeds, the emission will be affected by the surrounding field, and the contribution of the current pixel decreases. Therefore, the approximation error will be only in the first few pixels, and the emission converges to its "true" value eventually.

The deposited energy per time was implemented as the energy deposited by the electrons during a single-time step of the implicit Euler scheme used to update the electric field and the charge distribution, divided by the duration of that time step. This works fine if there are sufficiently many electrons per time step (say >100). However, Fig. 19 investigates the impact of the electric field update frequency and uses only 10 electrons per time step. For that investigation, we defined a timescale $\tau = \Delta t/3$ based on the time step Δt of the simulation with 100 electrons per time step.

The deposited energy $D(r, t_{n-1})$ for a given time step is then computed as follows:

$$D(r, t_n) = (1 - C) * A(r, t_n) + C * D(r, t_{n-1}), \qquad (12)$$

where the deposited energy from the previous time step is added damped by the factor $C = \exp(-\Delta t/\tau)$ and $A(r, t_n)$ describes the energy deposited by the electrons during that time step. We have $C = \exp(-3) = 0.05$ for the simulations with 100 electrons, and $C = \exp(-0.3) = 0.74$ for the simulation with 10 electrons.

Figure 19 compares the SE emission of Fig. 12(c) to the case when the electric field is updated with 10 times the frequency. In the first few pixels, the SE yield is generally slightly lower, but the signal drop is still present.

The electron–matter scattering models, i.e., elastic and inelastic scattering, used in this study are first principle models. Although they are based on established models, there are still model assumptions, especially at very low energies, which can lead to errors in SE emission. In addition, trapping and detrapping in insulators are well-known phenomena. Electrons and holes are trapped in defects, impurities, and dislocations. Electric fields and material heating can release the trapped electrons (detrapping) in case the added energy is greater than the trapping energy. Such kind of conduction mechanism is also known as Poole-Frenkel conduction.[49] To take that into account, many very low energy electrons should be traced to lower energies, even below the vacuum barrier height. The discrete modeling of these very low energy events would add a significant computational load since there is an excessive amount of electrons in this energy range. Furthermore, it is experimentally very hard to verify the cross-sections at very low energies. Although the first principle physics-based trapping/detrapping models will lead to a more accurate model, it is a very challenging task from

Downloaded From: https://www.spiedigitallibrary.org/journals/Journal-of-Micro/Nanolithography,-MEMS,-and-MOEMS on 06 Feb 2020
Terms of Use: https://www.spiedigitallibrary.org/terms-of-use

many perspectives: physics, characterization of material at hand, and computationally.

As mentioned in Sec. 1, in our previous simulation work,[20] we were not able to reproduce the smooth intensity drop seen in the experiments. There are two reasons for this: the lack of some essential model components and misinterpreting the experimental data. The latter was due to the tilt of the sample. The sharp signal drop on the oxide in Fig. 1(a) was first interpreted as a strong charging effect. However, we realized that the contrast change is mostly due to the sample tilt, the image being a combination of a complex topography and an asymmetric scattering cloud in the sample.[50] This sharp drop is not present in a common top-down image, as demonstrated in Figs. 13(a) and 13(b). In this case, the charging effect appears subtly, which could be most dangerous, according to Postek et al.[3] because it could be easily overlooked by a microscopist. After adding the missing model components, this phenomenon was reproduced, as demonstrated in Sec. 4.3. The linescans over an insulator in Sec. 4.2 are preliminary tests of the signal drop, which qualitatively agree with the (spot mode simulation) results in Fig. 4 of Ohya et al.,[36] and Fig. 4 of Ref. 10. However, experimental evidence is still missing for this case. An experimental dataset, as explained in Sec. 4.2, can be very useful to judge the effects of the models. This experiment can even be simplified to spot mode acquisition. Another related issue is the SE yield (curve) of SiO_2, which is dependent on current and time. Previously, Belhaj et al.[51] have conducted yield measurements on alumina (Al_2O_3). A similar study for SiO_2 is required to verify SE yields and the models.

In Sec. 4.4, the effect of the models was demonstrated in a setup, typical for voltage contrast imaging in electron beam testing technology. In the simulations, the effect of the EBIC model is observed as brightening of electrically conductive parts and its surrounding oxide [Fig. 17(d)]. Thong reported in Fig. 2.74 the brightening of passivation and oxide layers when the beam reaches a base-collector junction at higher energies.[52] Similarly, Leamy reported in Figure 23 that the imaged surface brightens due to the EBIC effect, revealing the location of a buried junction.[53] Besides, conducting a similar experiment can reveal the extent of EBIC effect more quantitatively.

Moreover, the beam deflection due to induced-charging has been studied[54] at 50 keV with the models explained in this work. Simulation results agree with experimental results qualitatively for most of the experiments, quantitatively in some cases.

In the simulations, Monte-Carlo calculations are fully scalable, meaning that using more cores would make the calculations faster. At present, the electric field calculations are parallelized on four CPU cores. In principle, the field solution can be parallelized with a higher number of cores, but, in practice, we did not achieve a higher gain because of the increasing communication cost. In a benchmarking test, we found that the open-source multigrid solvers in PETSc (i.e., BoomerAMG and GAMG) are scalable up to 16 threads and giving a factor of 2 to 3 speed-up for our test matrices.[55]

Using a more efficient grid (e.g., a triangular mesh) can speed up the calculations extra because the problem size will be much smaller (factor of 10). However, the speed-up is expected to be only a factor of 2 to 3 due to the increasing complexity of the solution in the multigrid regime.

6 Conclusions

Model improvements for Monte-Carlo simulations were presented. These improvements include both low energy electron scattering models and the charging of dielectrics. First of all, we have included first principle scattering models to simulate electron–matter interactions in order to predict charge distributions in the material more precisely. The latter involves models that couple dynamically with the charge distribution, such as calculation of local fields, tracing of the electrons in the field, and redistribution of the charges in the materials. For instance, the redistribution models, EBIC and dielectric breakdown, help to include induced conductivity in dielectric materials.

We have shown that including first principle scattering models, especially electron–phonon scattering leads to a more realistic charge distribution inside the material. Although the generation and tracing of every electron in the field increase the computation time significantly, we tried to avoid simplifications/optimization of the scattering models. However, for the fine adjustment of the yield, we have used empirically modeled trapping cross-sections.

In an earlier study, the charge mobility was not allowed in the dielectrics. This was causing accumulation of unrealistically big potentials, causing beam deflections. Introducing redistribution of the charges helped to solve these artifacts. The models incorporate tracing of all the electrons with a higher accuracy in the electric field, enabling us to reproduce contrast changes due to the surface potential. This results in better yields and more realistic energy analysis of the emitted electrons.

In addition, the EBIC model allowed simulation of induced conductivity effects, where the presence of the beam increases the conductivity of the dielectric material, creating a conductive channel to neighboring conductive materials at ground potential.

Future steps will include a more effective meshing technique to reduce the problem size to speed up the simulations. Improvements in the modeling can be considered by including surface plasmons and a physics-motived trapping and detrapping model. To quantify the effects and error bars, a proper parameter and model sensitivity analysis as well as good experimental results is needed.

Acknowledgments

We would like to thank Dr. Jens Bolten for his assistance and for providing experimental results. K.T.A. would like to express his sincere thanks to Dr. Thomas Verduin, Annemarie Theulings, and Luc van Kessel for fruitful discussions on the physics of the electron–matter interactions. T.K. is grateful to Dr. John Villarrubia for providing the source code of JMONSEL, which provoked the idea of the dielectric breakdown model. We also would like to thank Dr. Robert Polster for pointing out the role of charge imbalance to explain conductivity near the surface. We gratefully acknowledge GenISys-GmbH and RAITH B.V. for funding this research project. An earlier version of the work has been partially published in a SPIE Proceedings paper titled "Model improvements to simulate charging in SEM," https://doi.org/10.1117/12.2297478.

References

1. M. Kotera and H. Suga, "A simulation of keV electron scatterings in a charged-up specimen," *J. Appl. Phys.* **63**(2), 261–268 (1988).

Downloaded From: https://www.spiedigitallibrary.org/journals/Journal-of-Micro/Nanolithography,-MEMS,-and-MOEMS on 06 Feb 2020
Terms of Use: https://www.spiedigitallibrary.org/terms-of-use

2. A. Seeger, A. Duci, and H. Haussecker, "Scanning electron microscope charging effect model for chromium/quartz photolithography masks," *Scanning* **28**(3), 179–186 (2006).
3. M. T. Postek and A. E. Vladár, "Does your SEM really tell the truth? How would you know? Part 4: charging and its mitigation," *Proc. SPIE* **9636**, 963605 (2015).
4. T. Ichinokawa et al., "Charging effect of specimen in scanning electron microscopy," *Jpn. J. Appl. Phys.* **13**(8), 1272–1277 (1974).
5. N. Okai and Y. Sohda, "Study on image drift induced by charging during observation by scanning electron microscope," *Jpn. J. Appl. Phys.* **51**, 06FB11 (2012).
6. J. Cazaux, "On some contrast reversals in SEM: application to metal/insulator systems," *Ultramicroscopy* **108**(12), 1645–1652 (2008).
7. L. Reimer, *Scanning Electron Microscopy*, 2nd ed., Vol. 45, p. 127, Springer, Heidelberg (1998).
8. J. Orloff, *Handbook of Charged Particle Optics*, 2nd ed., CRC Press, Boca Raton (2009).
9. M. P. Davidson and N. T. Sullivan, "Investigation of the effects of charging in SEM-based CD metrology," *Proc. SPIE* **3050**, 226–242 (1997).
10. H. Abe et al., "Contrast reversal effect in scanning electron microscopy due to charging," *J. Vac. Sci. Technol. B* **27**(3), 1039–1034 (2009).
11. Y. G. Li, P. Zhang, and Z. J. Ding, "Monte Carlo simulation of CD-SEM images for linewidth and critical dimension metrology," *Scanning* **35**(2), 127–139 (2013).
12. J. P. Ganachaud and A. Mokrani, "Theoretical study of the secondary electron emission of insulating targets," *Surf. Sci.* **334**(1–3), 329–341 (1995).
13. H.-J. Fitting and M. Touzin, "Secondary electron emission and self-consistent charge transport in semi-insulating samples," *J. Appl. Phys.* **110**, 044111 (2011).
14. M. Cao et al., "Charging dynamics of a polymer due to electron irradiation: a simultaneous scattering-transport model and preliminary results," *Chin. Phys. B* **21**(12), 127901 (2012).
15. L. Grella et al., "Three-dimensional simulation of top down scanning electron microscopy images," *J. Vac. Sci. Technol. B* **22**(6), 3399 (2004).
16. S. Babin et al., "CHARIOT: software tool for modeling SEM signal and e-beam lithography," *Phys. Procedia* **1**(1), 305–313 (2008).
17. K. Ohya and H. Kuwada, "Modeling of electron beam charging of an insulating layer on a silicon substrate," *e-J. Surf. Sci. Nanotechnol.* **9**, 112–116 (2011).
18. E. Ilgüsatiroglu et al., "New integrated Monte Carlo code for the simulation of high-resolution scanning electron microscopy images for metrology in microlithography," *Proc. SPIE* **9050**, 90500I (2014).
19. J. S. Villarrubia et al., "Scanning electron microscope measurement of width and shape of 10 nm patterned lines using a JMONSEL-modeled library," *Ultramicroscopy* **154**, 15–28 (2015).
20. K. T. Arat et al., "Electric fields in scanning electron microscopy simulations," *Proc. SPIE* **9778**, 97780C (2016).
21. M. Kotera, K. Yamaguchi, and H. Suga, "Dynamic simulation of electron-beam-induced charging-up of insulators," *Jpn. J. Appl. Phys.* **38**(12B), 7176–7179 (1999).
22. F. Salvat, A. Jablonski, and C. J. Powell, "ELSEPA—Dirac partial-wave calculation of elastic scattering of electrons and positrons by atoms, positive ions and molecules," *Comput. Phys. Commun.* **165**(2), 157–190 (2005).
23. E. Kieft and E. Bosch, "Refinement of Monte Carlo simulations of electron-specimen interaction in low-voltage SEM," *J. Phys. D Appl. Phys.* **41**(21), 215310 (2008).
24. T. Verduin, "Quantum noise effects in e-beam lithography and metrology," Delft University of Technology, Delft (2016).
25. M. Winter, "WebElements," http://www.webelements.com (accessed 23 January 2018).
26. T. Gray and M. Whitby, "Periodictable.com," http://periodictable.com/Elements/029/index.html (accessed 23 January 2018).
27. W. M. Haynes, *CRC Handbook of Chemistry and Physics: A Ready-Reference Book of Chemical and Physical Data*, CRC Press, Boca Raton, Florida (2011).
28. S. O. Kasap, *Principles of Electronic Materials and Devices-TT*, 2nd ed., McGraw-Hill, Boston (2002).
29. J.-C. Kuhr and H.-J. Fitting, "Monte-Carlo simulation of low energy electron scattering in solids," *Phys. Status Solidi* **172**, 433–450 (1999).
30. B. J. Van Zeghbroeck, "Effective mass in semiconductors," *Principles of Semiconductor Devices*, 1997, https://ecee.colorado.edu/~bart/book/effmass.htm (9 January 2018).
31. E. Schreiber and H.-J. Fitting, "Monte Carlo simulation of secondary electron emission from the insulator SiO_2," *J. Electron. Spectrosc. Relat. Phenom.* **124**(1), 25–37 (2002).
32. O. Madelung, U. Rössler, and M. Schulz, "Silicon (Si), sound velocities: datasheet from Landolt-Börnstein—Group III Condensed Matter... Volume 41A1β: 'Group IV Elements, IV-IV and III-V Compounds. Part b—Electronic, Transport, Optical and Other Properties' Springer Materials (https://doi.org/10.1007/b80447?nosfx=y)," Springer-Verlag, Berlin, Heidelberg.
33. O. Madelung, U. Rössler, and M. Schulz, "Silicon (Si), deformation potentials: datasheet from Landolt-Börnstein—Group III Condensed Matter... Volume 41A1β: 'Group IV Elements, IV-IV and III-V Compounds. Part b—Electronic, Transport, Optical and Other Properties' in SpringerMaterials," Springer-Verlag, Berlin, Heidelberg.
34. D. Joy and S. Luo, "An empirical stopping power relationship for low-energy electrons," *Scanning* **11**(4), 176–180 (1989).
35. J. C. Ashley, "Interaction of low-energy electrons with condensed matter: stopping powers and inelastic mean free paths from optical data," *J. Electron. Spectrosc. Relat. Phenom.* **46**(1), 199–214 (1988).
36. K. Ohya et al., "Dynamic simulation of secondary electron emission and charging up of an insulating material," *Surf. Coatings Technol.* **202**(22–23), 5310–5313 (2008).
37. M. Dapor, "Monte Carlo simulation of secondary electron emission from dielectric targets," *J. Phys. Conf. Ser.* **402**, 012003 (2012).
38. T. Kaneko, "Energy distribution of secondary electrons emitted from solid surfaces under electron bombardment I. Theory," *Surf. Sci.* **237**(1–3), 327–336 (1990).
39. R. Kyng and S. Sachdeva, "Approximate Gaussian elimination for Laplacians—fast, sparse, and simple," in *IEEE 57th Annu. Symp. Found. Comput. Sci.*, pp. 573–582 (2016).
40. Y. Notay and P. S. Vassilevski, "Recursive Krylov-based multigrid cycles," *Numer. Linear Algebra Appl.* **15**(5), 473–487 (2008).
41. R. Tanaka, H. Sunaga, and N. Tamura, "The effect of accumulated charge on depth dose profile in poly(methylmethacrylate) irradiated with fast electron beam," *IEEE Trans. Nucl. Sci.* **26**(4), 4670–4675 (1979).
42. L. Grella, G. Lorusso, and D. L. Adler, "Simulations of scanning electron microscopy imaging and charging of insulating structures," *Scanning* **25**(6), 300–308 (2003).
43. K. Shadman and I. De, "Analytic models for the kinetics of generating a voltage contrast signal from contact plugs used in integrated circuits," *J. Appl. Phys.* **101**(6), 064913 (2007).
44. M. T. Postek and R. L. Watters, "Report of investigation: reference material 8820 scanning electron microscope scale calibration artifact," Material Measurement Laboratory, Gaithersburg, https://www-s.nist.gov/srmors/view_cert.cfm?srm=8820 (2009).
45. M. T. Postek et al., "Reference material (RM) 8820: a versatile new NIST standard for nanometrology," *Proc. SPIE* **7638**, 76381B (2010).
46. M. T. Postek et al., "Comparison of electron imaging modes for dimensional measurements in the scanning electron microscope," *Microsc. Microanal.* **22**(4), 768–777 (2016).
47. D. C. Joy and C. S. Joy, "Dynamic charging in the low voltage SEM," *Microsc. Microanal.* **1**(3), 109–112 (1995).
48. D. R. Lide, *CRC Handbook of Chemistry and Physics*, Internet V, CRC Press, Boca Raton, Florida (2005).
49. N. Cornet et al., "Electron beam charging of insulators with surface layer and leakage currents," *J. Appl. Phys.* **103**(6), 064110 (2008).
50. K. T. Arat et al., "Electron beam lithography on curved or tilted surfaces: simulations and experiments," *J. Vac. Sci. Technol. B* **37**(5), 051604 (2019).
51. M. Belhaj, T. Tondu, and V. Inguimbert, "Effect of the incident electron fluence on the electron emission yield of polycrystalline Al_2O_3," *Appl. Surf. Sci.* **257**(10), 4593–4596 (2011).
52. J. T. L. Thong, *Electron Beam Testing Technology*, Plenum Press, New York (1993).
53. H. J. Leamy, "Charge collection scanning electron microscopy," *J. Appl. Phys.* **53**, R51 (1982).
54. K. T. Arat et al., "Charge-induced pattern displacement in E-beam lithography," *J. Vac. Sci. Technol. B* **37**(5), 051603 (2019).
55. S. Balay et al., "PETSc web page," 2019, https://www.mcs.anl.gov/petsc (accessed 25 October 2019).

Kerim T. Arat is a PhD researcher at Delft University of Technology since November 2015. His research focuses on the development of Monte-Carlo simulations for scanning electron microscopy (SEM) and electron beam lithography (EBL) applications, such as 3D measurement with SEM, reducing charge-induced beam displacement in EBL.

Thomas Klimpel received his diploma degree in maths from TU Munich, in 2002. He worked on modeling and numerical methods for optical and EUV lithography at Sigma-C, which was bought by Synopsys, in 2006. Later, he worked on e-beam proximity effect correction, before he joined GenISys, in 2013. His current focus is on simulation of charging effects in scanning electron microscopy.

Cornelis W. Hagen received his master's degree (1983) and a PhD (1991) of the Free University of Amsterdam, the Netherlands. He was a researcher at Paul Scherrer Institute in Switzerland from 1989 to 1992, and at the Kamerlingh Onnes Laboratory of Leiden University, the Netherlands, from 1992 to 1994. In 1994, he joined Delft University of Technology as an assistant professor and was appointed as an associate professor in 2008. His area of research is microscopy and lithography with charged particles.

Downloaded From: https://www.spiedigitallibrary.org/journals/Journal-of-Micro/Nanolithography,-MEMS,-and-MOEMS on 06 Feb 2020
Terms of Use: https://www.spiedigitallibrary.org/terms-of-use